J Mater Sci (2011) 46:2112–2122
DOI 10.1007/s10853-010-5047-6

Morphology and mechanical properties of isotactic polypropylene glass mat thermoplastic composites modified with organophilic montmorillonite

S. Dalle Vacche · C. J. G. Plummer · C. Houphouët-Boigny · J.-A. E. Månson

Received: 17 May 2010 / Accepted: 1 November 2010 / Published online: 18 November 2010

Abstract Satisfactory impregnation of glass fiber mats may be obtained with isotactic polypropylene/montmorillonite (MMT) nanocomposites under conditions comparable with industrial conditions. However, it is demonstrated here that the high melt viscosity of the nanocomposite matrix at low shear rates may significantly influence the release of the compressive load in the glass mat and hence the glass fiber distribution in consolidated specimens. Thus, depending on the initial lay-up and overall glass fiber content, the bending modulus may either increase or decrease with increasing MMT content, whereas the tensile modulus is more consistent with micromechanical models assuming a uniform glass fiber distribution. Results from fractographic analyses show that the presence of matrix rich layers at the specimen surfaces may also lead to premature crack initiation and failure in flexion.

Introduction

Glass mat reinforced thermoplastic (GMT) composites have been widely used in structural and semi-structural applications since the early 1970s, thanks to their high specific stiffness, strength and impact resistance [1]. In principle, any thermoplastic polymer may be used as a matrix for GMT, but in practice over 95% of production is based on isotactic polypropylene (iPP). The glass mats may be composed of continuous fibers (swirl mats) or discontinuous long fibers (chopped fiber mats), and the GMT sheets are manufactured by melt impregnation or the slurry deposition (papermaking) process [2]. The mechanical properties of iPP-based GMT composites are well known to depend strongly on their morphology and processing conditions, and differences in the mechanical response of GMT fabricated with continuous or discontinuous fiber mats have been evidenced [3–10]. A variety of techniques have been used to investigate the corresponding failure mechanisms and the development of the damage zone, including in situ optical microscopy, acoustic emission, and infrared thermography [11–18].

The recent commercialization of organically modified montmorillonite (MMT) clay/iPP concentrates formulated to improve the compatibility of the MMT with the iPP matrix has raised the possibility of hybrid iPP nanocomposite GMT materials. The presence of MMT has potential benefits not only for the matrix mechanical properties but also for a range of other properties, such as the heat distortion temperature and flame retardance [19–21]. Furthermore, fiber–matrix interfacial adhesion may also be enhanced by addition of clay [22, 23]. However, there have to date been relatively few investigations of the properties and processing of hybrid fiber-reinforced composites with nanocomposite polymer matrices, and most of these have centered on thermoset nanocomposites reinforced with glass or carbon fibers [24–31]. Significant improvements in flexural stiffness have been reported for glass fiber-reinforced composites with PA6/clay (MMT or hectorite) [32] and iPP/mica [33] matrices, and the feasibility of using an iPP/MMT matrix to manufacture hybrid iPP/MMT GMT composites with improved stiffness at the laboratory scale has recently been established [34, 35]. On the other hand, if mass production of hybrid GMT nanocomposites is to be envisaged, cost efficiency of the manufacturing process is a

S. Dalle Vacche · C. J. G. Plummer · C. Houphouët-Boigny · J.-A. E. Månson (✉)
Laboratoire de Technologie des Composites et Polymères (LTC), Ecole Polytechnique Fédérale de Lausanne (EPFL), 1015 Lausanne, Switzerland
e-mail: jan-anders.manson@epfl.ch

driving factor, so that it is important to maintain processing conditions representative of those used for current industrial materials. A key process in the production of GMT components is the preparation of semi-finished GMT sheets, known as blanks, which involves the infiltration of the glass mat by the molten polymer matrix under moderate pressure, followed by release of the compressive load in the glass fiber mat [36]. As discussed in what follows, in the case of infiltration of needled glass fiber mats by an iPP matrix, the unloading time of the glass fiber mat may be much longer than the infiltration time. If the processing time is too short, an inhomogeneous distribution of the fibers may therefore persist even in an apparently well-impregnated part [37], with possible consequences for mechanical properties, particularly in flexion. This effect is expected to be even more marked in the case of an iPP/MMT matrix, since the melt viscosity at low shear rates, typical of the final stages of impregnation, is known to increase significantly with MMT content [35, 38], possibly leading to much longer unloading times. The present work is aimed at investigating the extent and consequences of incomplete release of the compressive load in the fiber mat in a series of GMT specimens prepared from iPP and iPP/MMT and fully consolidated in a single processing step. The distribution of the glass fibers and the MMT has been carefully characterized in each case, and the Cox–Krenchel model and the classical beam theory used to relate the observed tensile and flexural moduli to the morphology. Fractographic analysis has also been carried out to account for the evolution of the tensile and flexural strength.

Experimental

Materials and processing

The matrix was a GMT grade iPP with a density of 0.9 g cm^{-3}, kindly provided by a major GMT supplier, and whose rheological response has been described in a previous publication [35]. The MMT was incorporated in the form of a Nanomer® C.44PA iPP concentrate (Nanocor, Inc., Arlington Heights, Illinois, USA), containing 40–50 wt% of Nanomer® I.44PA clay, which is reported to be MMT organically modified with a dimethyldialkylammonium halide [39], a polymeric compatibilizer (the nature of which was not disclosed by the supplier) and an iPP carrier resin. Ashing of the concentrate, by heating in a Carbolite furnace (Carbolite, UK) at 500 °C for 2 h, indicated an inorganic content of 27 wt%. The iPP and the MMT concentrate were dried overnight at 80 °C and then melt compounded and pelletized using a 16 × 15D twin screw extruder (PRISM TSE-16-TC, Thermo Fisher Scientific Inc., Switzerland), equipped with a single-hole strand die (screw speed 20 rpm, temperatures in the three zones from the feeder to the die set to 180, 200, and 200 °C, respectively). As reported previously [34], the homogeneity of the MMT dispersion improved at higher concentrations. A masterbatch containing 80 wt% iPP and 20 wt% Nanomer® C.44PA concentrate (leading to a concentration of 5.4 wt% inorganic MMT in the masterbatch) was therefore prepared, and the lower MMT concentration obtained by diluting the masterbatch with iPP in a second compounding step. Extrusion calendering was used to obtain films. The granulates were fed into the same PRISM extruder as used for compounding, but the strand die was replaced with a film die (die head set to 200 °C, other extrusion parameters as previously) coupled to a PRISM TSE Systems calendar (Thermo Fisher Scientific Inc., Switzerland). The calender temperature and speed were 25 °C and 1 rpm, respectively, and the distance between the rotating cylinders was adjusted to 0.5 mm, which led to a final thickness of 0.75 mm owing to die swell. The materials obtained in this way, containing 0, 3.3, and 5.4 wt% MMT will be referred to as iPP, iPP3.3, and iPP5.4, respectively.

A TP50 table-top press (Fontijne Holland, Netherlands) equipped with a 140 mm × 60 mm closed mold was used to manufacture compression molded plaques of iPP, iPP/MMT, and GMT. The glass fiber reinforcement for the GMT was provided by a 4 mm 2D needled glass fiber mat (Quadrant Plastics Composites, Lenzburg, Switzerland), with a fiber length of ∼50 mm and fiber diameter of 15 μm arranged in bundles of about 100 fibers. The surface density of the mat is 600 g m^{-2}. The compression molding cycle consisted of heating the materials to 200 °C over 10 min, holding at 200 °C for a further 10 min and then rapid cooling to 25 °C. The applied pressure was 1.2 MPa. Plaques of iPP and iPP/MMT were obtained by compression molding of three layers of the polymer films produced as described above. GMT plaques were produced from three layers of polymer film and two layers of dry glass fiber mat, stacked as shown in Fig. 1a. Specimens for flexural tests were also molded using a modified stacking sequence, in which the three layers of polymer film were placed between two layers of glass fiber mat (Fig. 1b).

Because the glass mats are known to be inhomogeneous, local differences in fiber density may induce a variation in the true fiber volume fraction in relatively small specimens

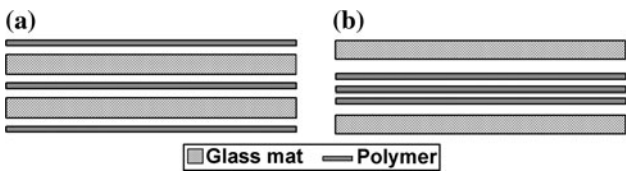

Fig. 1 Structure of the GMT preforms: **a** standard stacking sequence and **b** modified stacking sequence

Table 1 Characteristics of the different sets of GMT plaques

Designation	ϕ_f (%)		Mechanical test procedure
	Avg.	St. Dev.	
Set 1	16.0	0.01	Tensile
Set 2	15.6	0.04	Bending
Set 3	16.9	0.04	Bending
Set 4 (modified stacking sequence)	16.1	–	Bending

such as those used in the present study, which may have important consequences for the measured mechanical properties. The masses of the polymer films and glass fibers used for the manufacture of each GMT compression molded plaque were therefore carefully adjusted so as to produce sets of plaques with constant fiber contents. Three sets of GMT plaques (two to three plaques for each MMT concentration) molded with the standard stacking sequence were prepared in this way. A fourth set consisted of one iPP5.4 GMT plaque molded with the modified stacking sequence in Fig. 1b. The corresponding fiber volume fractions, ϕ_f, are given in Table 1 along with the standard deviation in ϕ_f. Three to four specimens were machined from each plaque as described under "mechanical testing". The ϕ_f for the individual specimens were determined by ashing and were found not to deviate by more than 10% from the values given in Table 1.

Morphology

An Olympus BX61 (Olympus Schweiz AG, Switzerland), microscope equipped with an F-view II Soft Imaging System black and white camera and a motorized stage was used to obtain optical micrographs of polished sections through the GMT plaques and image analysis software (ImageJ, U.S. National Institutes of Health, USA) was used for determination of the fiber and void distributions. To minimize fiber damage, the specimens were manually polished on a Struers Rotopol-1 polisher with SiC 1000, SiC 2400, and SiC 4000 grit grinding paper. Plasma and chemical etching of polished sections were used to reveal the MMT dispersions in the plaques [40, 41]. Plasma etching was performed in a Model 1020 Plasma Cleaner (E.A. Fischione Instruments Inc., USA) using a low-energy, inductively coupled, high frequency (HF) plasma, generated with a gas composed of 75% argon and 25% oxygen. Chemical etching was performed with an etching solution containing 32.7% H_3PO_4, 64.3% H_2SO_4, and 3% $KMnO_4$ followed by rinsing in distilled water and in H_2O_2. In both cases the specimens were sonicated in acetone after etching to remove the debris and then coated with a 15–30 nm layer of carbon to prevent charging. They were observed using a Philips XL30 FEG scanning electron microscope (SEM).

Mechanical testing and fractography

The elastic moduli and strengths of the nanocomposites and of the GMTs were measured in tension and three-point bending at room temperature using a screw driven UTS testing machine (Testsysteme Gmbh, Germany) equipped with a 1 kN load cell. For both the tensile and three-point bending tests, at least six specimens per material were tested, and the average and standard deviation of the results calculated. The experimental error was assumed to be twice the standard deviation. The tensile tests were performed at 2 mm/min according to the ASTM D638-91a standard. Dumbbell-shaped specimens with the ASTM D638 specimen IV dimensions were cut from the compression molded plaques and the tensile elastic modulus, E, was taken to be the slope of the initial linear part of the stress–strain curve. The fracture surfaces were carbon coated and observed by SEM, as described above. The three-point bending tests were carried out at 1 mm/min according to the ASTM D790-86 standard. Rectangular specimens of length $l = 60$ mm and width $b = 25$ mm were cut from the plaques following the recommendations in Table 1 of ASTM D 790-86. The support span L was 36 mm for the nanocomposite plaques and 40 mm for the GMT, so that the ratio of the support span to the thickness L/d was roughly 16 in each case, the plaque thicknesses d being of the order of 2.1–2.2 mm for the nanocomposite plaques and 2.5–2.7 mm for the GMT plaques. For the determination of the flexural modulus an LVDT sensor was placed below the specimen to record its true deflection. The flexural modulus, E_b, was calculated from:

$$E_b = \frac{L^3 m}{4bd^3} \tag{1}$$

where m is the stiffness, calculated as the slope of the tangent to the initial linear part of the load–deflection curve. The flexural strength S was calculated from the maximum load, P_{max}, according to:

$$S = \frac{3P_{max}L}{2bd^2} \tag{2}$$

and the strain r corresponding to each deflection D was taken to be

$$r = \frac{6Dd}{L^2} \tag{3}$$

To observe internal damage occurred in the three-point bending tests, 15×10 mm^2 samples were removed from the central area of the specimens where the fracture took

place. The samples were embedded in epoxy resin and polished as described previously.

Experimental results

Morphology

The porosity was found from optical micrographs to be 2–3 vol.% regardless of the matrix composition. A relatively homogeneous through-thickness fiber distribution was observed for the pure iPP matrix, with a local fiber volume fraction comparable to the average fiber volume fraction throughout the thickness of the specimens. For iPP3.3, the fiber volume fraction in the surface layers of the specimens was significantly reduced, and for iPP5.4 the bottom layers of the specimens were entirely free of fibers, as apparent from the optical micrographs of longitudinal sections shown in Fig. 2a–c. The corresponding through-thickness glass fiber distributions are shown in Fig. 3. An optical micrograph of an iPP5.4 GMT from set 4 (modified lay-up) is shown in Fig. 2d, where fiber-rich region at the outer surfaces and a fiber-poor region at the center of the specimen are visible.

SEM images of etched sections of the nanocomposite GMT showed the MMT to be uniformly distributed in the polymer matrix. It was also confirmed that no filtration of the MMT by the glass fiber mat took place during impregnation as the MMT was present close to the fiber surfaces and within the fiber bundles (Fig. 4a). No systematic orientation of the MMT platelets was observed, suggesting that any orientation present originally in the polymer films as a result of the extrusion step was lost after the compression molding step (Fig. 4b).

Tensile properties

A certain level of pre-stress was apparent from the stress–strain curves obtained from the tensile tests, which was inevitable in such measurements, but remained well within the elastic limit. At significantly higher strains, however, tensile stress–strain curves of compression molded iPP and iPP/MMT specimens (Fig. 5) became markedly non-linear. All the matrix materials showed brittle failure, with E increasing, and the strain at break and tensile strength decreasing with increasing MMT content (Table 2).

Typical stress–strain curves for tensile GMT specimens from set 1 (see Table 1) with different MMT concentrations in the matrix are given in Fig. 6. The stress–strain curves of the nanocomposite GMT also showed a number of small drops in stress prior to the point of maximum

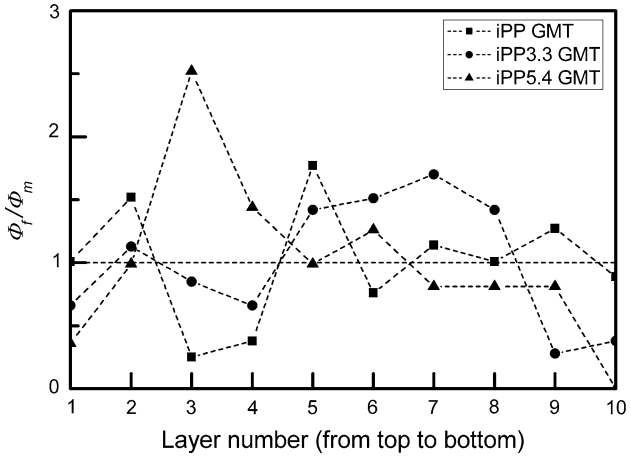

Fig. 3 ϕ_f normalized with respect to the overall mean fiber volume fraction ϕ_m for successive layers (numbered from *top* to *bottom*) through the thickness of the GMT specimens of set 2

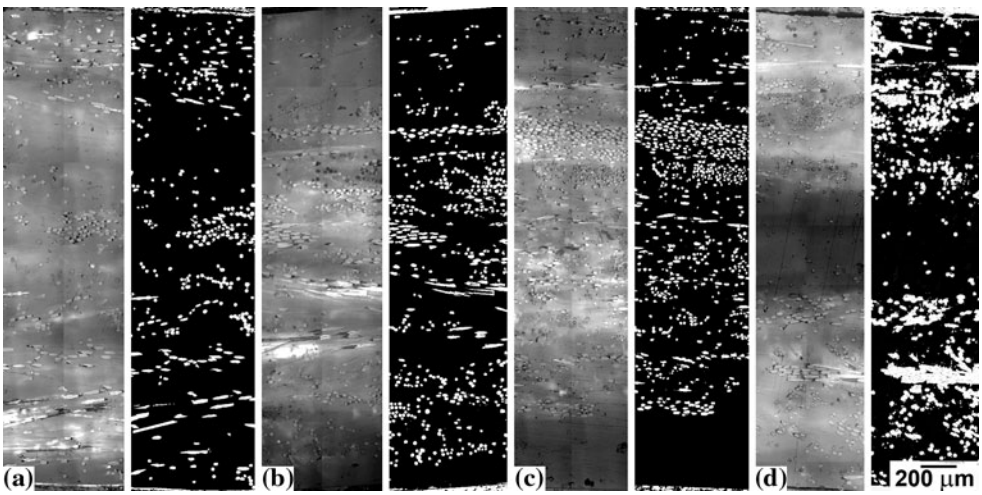

Fig. 2 Optical micrographs and corresponding binary images of polished longitudinal sections of specimens from set 2 **a** iPP GMT, **b** iPP3.3 GMT, **c** iPP5.4 GMT, and **d** an iPP5.4 GMT specimen from set 4

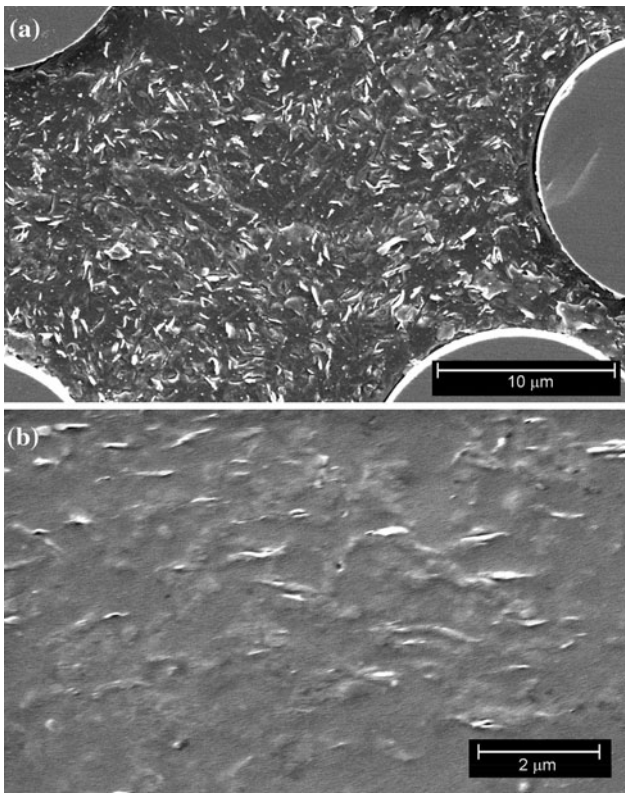

Fig. 4 SEM images of **a** chemically etched section of iPP5.4 GMT showing MMT uniformly distributed also near the glass fibers and **b** plasma etched section of iPP5.4 GMT showing randomly aligned MMT

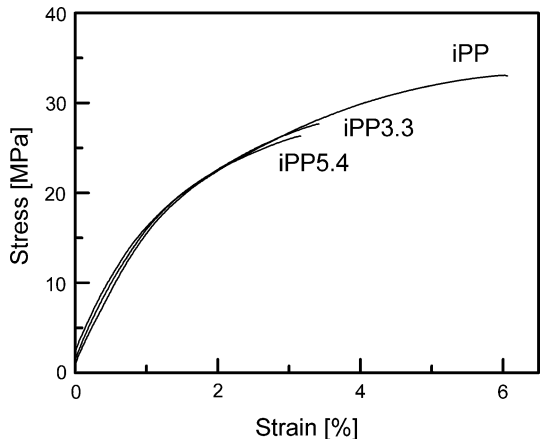

Fig. 5 Stress–strain curves obtained during tensile tests on compression molded specimens of iPP and iPP/MMT nanocomposites

stress. This was not observed for the iPP GMT. Acoustic emission results from Karger-Kocsis et al. [12] indicate that these drops are associated with crack growth and bifurcation, suggesting that damage starts before the maximum stress point. For all the GMT specimens the stress–strain curve showed a maximum prior to complete failure, and visual inspection during the tensile tests

Table 2 Mechanical properties of compression molded specimens of iPP/MMT nanocomposites

MMT (wt%)	Young's modulus (GPa)	Flexural modulus (GPa)	Tensile strength (MPa)	Flexural strength (MPa)
0	1.6	2.1	33.3	55.1
3.3	1.8	2.4	27.8	42.1
5.4	1.9	2.6	26.4	39.9

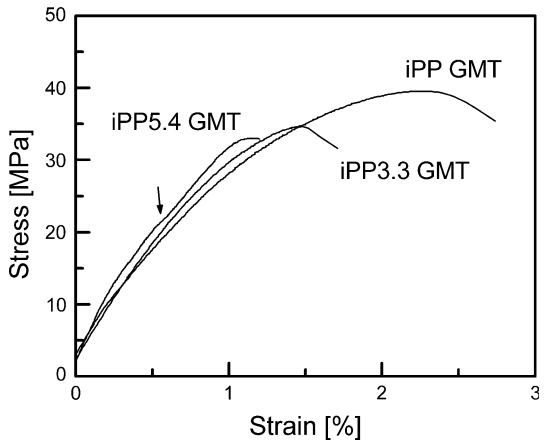

Fig. 6 Stress–strain curves typically obtained during tensile test on GMT specimens of set 1; the *arrow* indicates a small drop in stress associated with the onset of subcritical damage

indicated this to correspond to failure of the matrix and/or to fiber pull-out. Beyond the stress maximum, extensive fiber pull-out was observed, the fibers continuing to bridge the fracture surfaces up to complete failure. The fibers were pulled out to a greater extent in the pure iPP GMT than in the iPP/MMT-based GMT, in which the fibers failed soon after the stress maximum, leading to a substantial reduction in strain to break. As shown in Table 3, the average value of E increased slightly with MMT concentration, although the increase may not be significant in view of the large experimental error. The experimental error was attributed to variations in the fiber content within individual specimen sets owing to the inhomogeneity of the glass fiber mat, which has a relatively large effect in the tensile specimens, owing to their reduced cross-sections. The tensile strength (Table 3) of the iPP/MMT-based GMT materials was lower than that of the iPP GMT.

Flexural properties

The load–displacement curves typically obtained from the three-point bending test showed an initial toe region, which is an artifact due to settling of the specimens on the supports at the beginning of the test. After the toe region, a linear elastic regime could be identified, from which it was

Table 3 Mechanical properties of GMT specimens

MMT (wt%)	Set	Young's modulus (GPa)		Flexural modulus (GPa)		Tensile strength (GPa)		Flexural strength (MPa)	
		Avg.	St. Dev.	Avg.	St. Dev.	Avg.	St. Dev.	Avg.	St. Dev.
0	1	3.4	0.5			40.5	6.9		
3.3	1	3.6	0.4			34.8	6.1		
5.4	1	4.3	0.8			35.9	4.4		
0	2			4.8	0.2			96.8	6.6
3.3	2			3.9	0.3			77.1	8.1
5.4	2			4.1	0.4			80.1	5.1
0	3			5.6	0.3			114.3	7.7
3.3	3			5.4	0.4			108.5	9.9
5.4	3			5.1	0.3			101.1	4.9
5.4	4			7.1	0.4			131.6	13.5

possible to calculate the elastic modulus in bending, E_b, followed by a non-linear region. Because Eq. 2 for the calculation of the stress in the outer fibers is only valid for materials for which the stress is linearly proportional to the strain up to rupture. In the present case, therefore, Eq. 2 leads to systematic underestimates of the stress in the outer fibers.

The stress–strain curves obtained for compression molded iPP and iPP/MMT are shown in Fig. 7. The linear regime extended up to a deflection of 1 mm (1% strain) for the pure iPP, but was more restricted for the iPP/MMT nanocomposites. The bending modulus E_b increased slightly with increasing MMT concentration, while the strength and the strain at break decreased (Table 2).

Examples of the stress–strain curves typically obtained for the GMT composites with different MMT concentrations in three-point bending are shown in Fig. 8, and the results for E_b and the flexural strength for sets 2, 3, and 4 are summarized in Table 3. The stress–strain curves showed significant non-linearity at high strains. For all materials it was possible to identify a stress maximum, and this stress maximum appeared at lower strains in the iPP/MMT-based materials. As in the tensile tests, small drops in stress were observed in the stress–strain curves prior to the stress maximum for all the GMT with standard lay-up. However, this behavior was not observed for the GMT specimens with modified lay-up. The iPP/MMT-based GMT also showed a relatively abrupt decrease in stress beyond the stress maximum. For the specimens with standard lay-up, the strength, taken to be the maximum stress, decreased with MMT concentration. Sets 2 and 3 both showed lower E_b in the presence of MMT (the differences in the absolute values of the moduli measured for these two sets were accounted for by the difference in fiber volume fraction). Although the differences in modulus with MMT content were not statistically significant for set 3, owing to the large scatter in the data, they were significant for set 2. The iPP5.4 GMT from set 4 (iPP5.4m GMT),

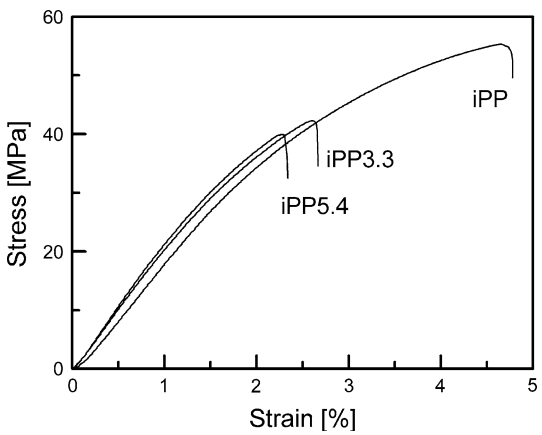

Fig. 7 Stress–strain curves obtained from three-point bending tests on compression molded specimens of iPP and iPP/MMT nanocomposites

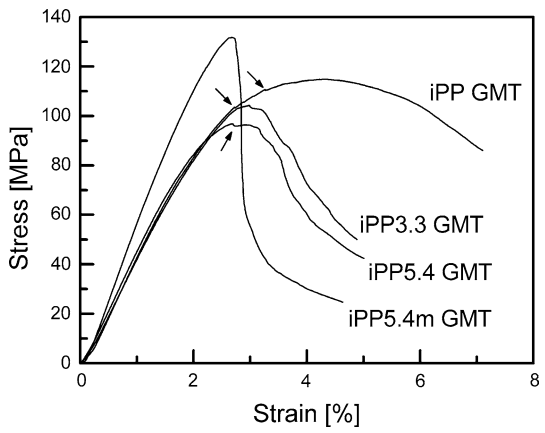

Fig. 8 Stress–strain curves typically obtained from three-point bending test on GMT specimens with standard lay-up (iPP, iPP3.3, and iPP5.4 GMT) and modified lay-up (iPP5.4m GMT); the *arrows* indicate small drops in stress associated with the onset of subcritical damage

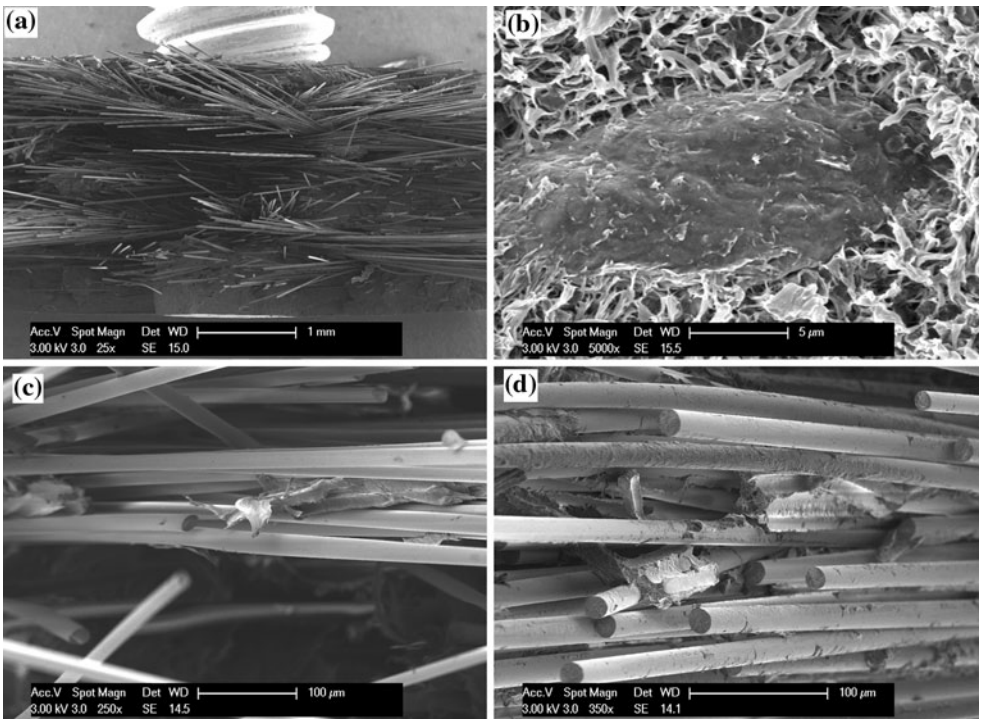

Fig. 9 SEM micrographs of: **a** fracture surface of an iPP5.4 GMT tensile specimen; **b** detail of the fracture surface from an iPP5.4 GMT tensile specimen, showing a large MMT aggregate; **c**, **d** surfaces of the glass fibers pulled out from the matrix in the fractured tensile specimens of iPP GMT and iPP5.4 GMT, respectively

which had a different fiber distribution, with most of the fibers concentrated in the outer layers of the specimens, showed substantially higher E_b and flexural strength than the other materials. The strain corresponding to the stress maximum was similar to that in the iPP/MMT GMT with the standard lay-up, but the decrease in stress after the maximum was more abrupt.

Fracture surfaces and fractography

The fibers visible at the fracture surface of iPP GMT tensile specimens showed a relatively homogeneous through-thickness distribution, while the nanocomposite GMT specimens showed areas of matrix with a relatively low fiber concentration in the outer layers, as well as at the center of the specimens (as shown for iPP5.4 GMT in Fig. 9a). In the areas where the fiber density was low it was possible to distinguish the fracture surface of the matrix, which was very rough, in the case of the nanocomposite GMT specimens. Furthermore, some large MMT clusters were also visible in the matrix (Fig. 9b). The surfaces of the glass fibers pulled out from the iPP matrix were smooth (Fig. 9c), indicating weak adhesion between the matrix and the fibers. The surface of the fibers pulled out from the matrix of the nanocomposite GMT, on the other hand, showed significant polymer residues, and, in the case of the iPP5.4 GMT, relatively large matrix fragments were also visible (Fig. 9d), suggesting better adhesion between the fibers and the matrix in the presence of MMT.

Images of the fractured specimens from three-point bending test are shown in Fig. 10. The maximum applied strain, calculated according to Eq. 3, was 5% for all the specimens, except that shown in Fig. 10b, for which it was 7%. In the iPP GMT specimens strained to 5% (Fig. 10a) the main crack initiated at the bottom surface at the mid-span, where the tensile strain reached a maximum, and a number of sub-critical microcracks and regions of more diffuse matrix deformation were also visible in the regions adjacent to the main crack, whereas little damage was visible at the upper surface. The subcritical damage in the matrix mostly originated from glass fiber debonding, and some debonded glass fibers were also visible at the surfaces of larger cracks (as indicated in the inset of Fig. 10a). When the sample was strained to 7% (i.e., up to the strain at break) the main crack propagated from the bottom surface through the center of the specimen, and deformation was also visible at the upper surface (Fig. 10b). Substantial subcritical damage continued to be present in the regions surrounding the main crack, including debonded fibers and fibers bridging the crack faces.

In the nanocomposite GMT with the standard fiber lay-up strained to 5% (Fig. 10c), the main crack propagated over two-thirds of the specimen width, starting with a relatively straight trajectory from the bottom surface,

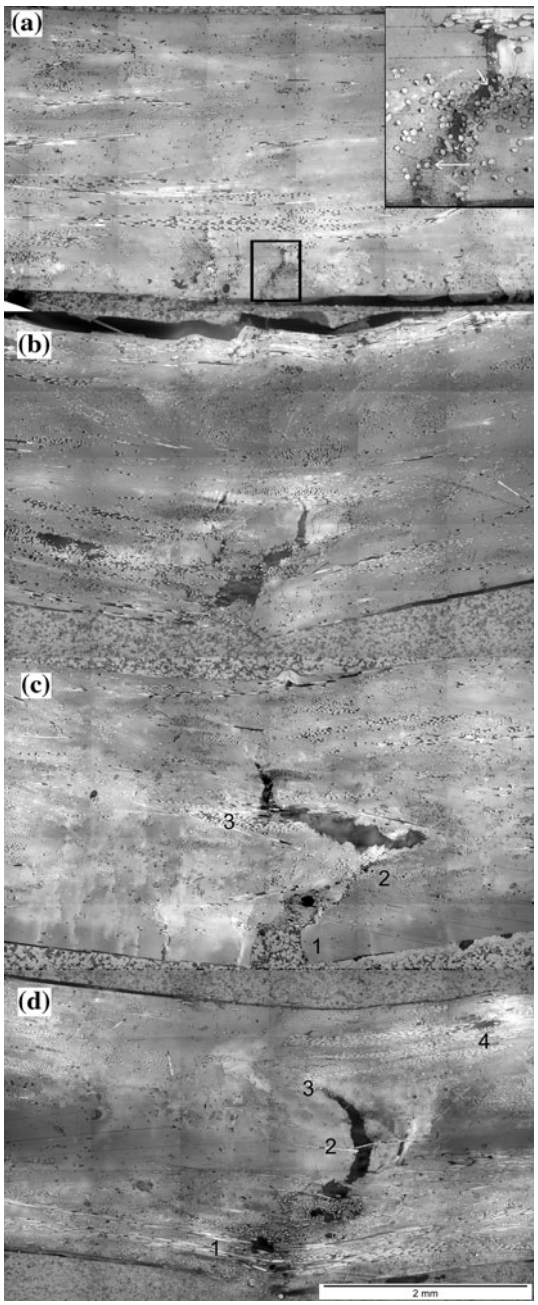

Fig. 10 Optical micrographs of three-point bend specimens: **a** iPP GMT strained to 5%: cracks are visible at the bottom surface, the *inset* shows a detail of one of these cracks; **b** iPP GMT strained to 7%; **c** iPP5.4 GMT strained to 5%: the crack trajectory is straight in the areas poor in fibers (*1*) and deviates in the areas rich in fibers (*2* and *3*); **d** iPP5.4 GMT with the modified stacking sequence strained to 5%, showing: (*1*) fibers pulled out from, or bridging the crack surfaces at the bottom surface; (*2*) a straight trajectory in the central area poor in fibers, (*3*) crack arrest, (*4*) internal cracking at upper surface

where the fiber density was relatively low, deviating in regions richer in fibers, and resuming its initial trajectory in matrix-rich regions further into the specimen. Substantial subcritical damage was again visible around the main crack and was also present in regions relatively far from the main crack. Cracking and other forms of damage were particularly extensive for the iPP5.4 GMT, with subcritical damage widespread in regions well away from the main crack. Of particular interest was the presence of a number of smaller cracks running parallel to the main crack in the matrix-rich bottom surface layer and which were arrested by the adjacent fiber-rich layer. The damage at 5% strain of the iPP5.4 GMT with the modified stacking sequence (fibers concentrated near the surfaces) was substantially different from those described above (Fig. 10d). Also in this case, the main crack penetrated through more than two-thirds of the specimen. The fracture near the bottom surface was similar to that observed for the iPP GMT, in that several fibers were pulled out from, or bridged the crack faces. On reaching the matrix-rich central part of the specimen, the crack assumed a straight trajectory, and was arrested by the adjacent fiber-rich region. Subcritical damage was clearly visible near the fracture surfaces in the matrix-rich regions. Internal cracking was also present near the upper surface, which was deformed in compression.

Modeling of tensile and flexural moduli

The Young's modulus E may be calculated for GMT specimens from the matrix and fiber moduli. In this case, the rule of mixtures for unidirectional composites is modified to take into account the "shear lag" effect, following Cox and Krenchel [42–44], so that

$$E = \eta_0 \eta_L \phi_f E_f + (1 - \phi_f) E_m \quad (4)$$

where ϕ_f is the volume fraction of the fibers and E_f and E_m are the Young's moduli of the fibers ($E_f = 76$ GPa [26]) and of the matrix (taken from Table 2), respectively. The fiber orientation factor η_0 takes into account the random orientation, for which many fibers contribute only partially to the modulus in directions to which they lie at a large angle. The glass mat used in this study had a random 2D in-plane arrangement of the fibers ($\eta_0 = 0.375$) but was also expected to show some 3D orientation ($\eta_0 = 0.2$) owing to the needling [45]. Therefore, the modulus was expected to lie between the limiting moduli estimated using these two values for η_0. The fiber length efficiency factor, η_L, which depends on the aspect ratio of the fibers may be taken to equal 1 [42]. The limiting E calculated from Eq. 4 are shown in Fig. 11a, and the lower limit ($\eta_0 = 0.2$) is more consistent with the data, confirming significant out-of-plane fiber orientation, due to the needling of the glass mat.

The same model based on a homogeneous glass fiber distribution would also imply a slight increase in E_b with increasing MMT content, while experimentally the opposite is observed. Classical beam theory is therefore invoked to take into consideration the fiber distribution gradients

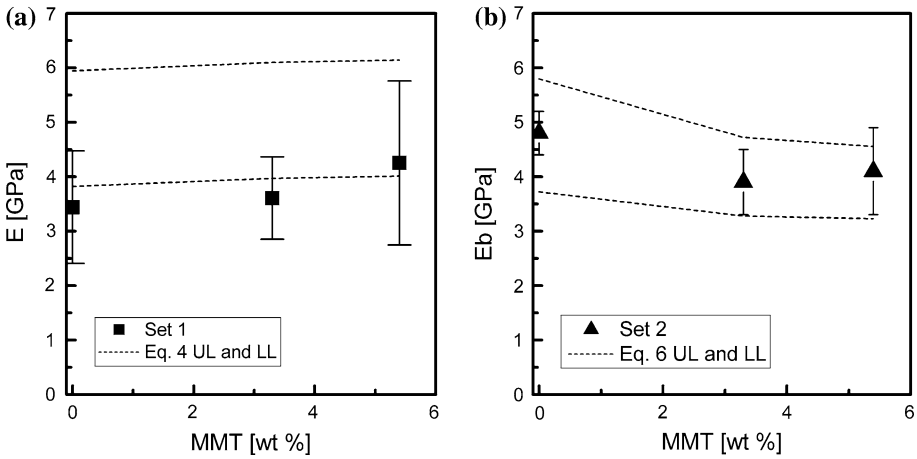

Fig. 11 **a** Young's modulus in tension of GMT specimens and upper (UL) and lower (LL) limits for the modulus calculated with the Cox-Krenchel rule of mixtures (Eq. 4) and **b** flexural modulus of GMT specimens of set 2 and corresponding UL and LL calculated with the beam theory (Eq. 6)

and account quantitatively for the results for E_b. A specimen with a non-uniform distribution of the fibers through its thickness may be represented as a laminate beam composed of layers in which the fiber distribution, and all other properties, can be considered homogeneous. The flexural rigidity D, defined as the product of the modulus E and the moment of inertia I, is then given for the laminate beam by the sum of the flexural rigidities of each layer:

$$D_{tot} = \sum_i (EI)_i = \frac{E_1 t_1^3}{12} + \frac{E_2 t_2^3}{12} + \frac{E_3 t_3^3}{12} + E_1 t_1 \left(\frac{t_1}{2} + t_2 + \frac{t_3}{2} - e\right)^2 + E_2 t_2 \left(\frac{t_2}{2} + \frac{t_3}{2} - e\right)^2 + E_3 t_3 e^2 \quad (5)$$

where E_i and t_i, respectively, indicate the Young's modulus and thickness of each layer, and e is the distance from the neutral axis of the beam to the centroid of the bottom layer. The effective flexural modulus of the beam is then obtained from:

$$E_b = \frac{1}{I_{tot}} \sum_i (EI)_i \quad (6)$$

For the specimens of set 2, the average thickness and fiber concentration of the layers were determined by optical microscopy and are summarized in Table 4.

The minimum and maximum values of the Young's modulus, E_i^{min} and E_i^{max}, were then calculated for each layer according to Eq. 4 taking η_0 equal to 0.2 and 0.375, respectively. The results obtained by introducing these values into Eq. 5 and then calculating the effective flexural moduli from Eq. 6 are shown in Fig. 11b. The calculated values in this case decreased with MMT content owing to the non-uniform fiber distributions, and the experimental values lay between the minimum and maximum calculated values.

Table 4 Thickness and fiber volume fraction of the layers of the laminate beams

Layer	iPP GMT		iPP3.3GMT		iPP5.4GMT	
	t (mm)	ϕ_f (%)	t (mm)	ϕ_f (%)	t (mm)	ϕ_f (%)
1	2.6	15.6	0.35	3.7	0.51	9.6
2	2.6	15.6	1.77	20.5	1.72	21.4
3	2.6	15.6	0.48	10.7	0.36	0

Discussion

The values of the tensile moduli for the iPP and IPP/MMT compression molded specimens (Table 2) were somewhat lower than those measured for the corresponding extrusion calendered films, but similar to those obtained for specimens injection molded from the compounded granulates for comparable compositions [34], consistent with a loss of any orientation in the polymer chains and/or the MMT particles induced during the extrusion step. The decrease of strength and elongation at break is attributed to the presence of large MMT aggregates in the matrix, as concluded by Li et al. [46]. The same considerations apply to the results of the flexural tests.

The differences in glass fiber distribution in the GMT specimens with different MMT loading may be explained in terms of the impregnation process, as modeled by Michaud and Månson and shown schematically in Fig. 12 [37]. First the polymer matrix and the preformed glass mat are heated to above the softening point of the polymer matrix, and then the materials are subjected to an external pressure ($t = 0$). When the external pressure is applied the fiber mats are compressed and the molten matrix starts to infiltrate the fibers ($0 < t < t_{fin}$). During impregnation the matrix initially infiltrates the voids between the fiber bundles. This is followed by wetting of the individual fibers in the bundles and infiltration of the inter-fiber voids. As the

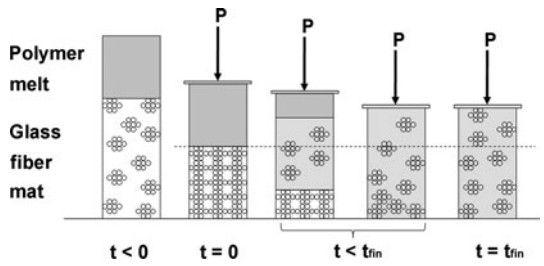

Fig. 12 Schematic representation of the impregnation process [37]

melt front advances the fiber mat begins to recover its initial shape while the compressive load on the fiber mat decreases. At intermediate stages of this process, the fiber volume fraction is non-uniform along the infiltration direction, but after a certain time t_{fin}, given sufficient space in the mold, the fiber mat is able to unload fully. If not, it remains in compression. In either case, the fiber volume fraction associated with the mat is expected to be relatively uniform after solidification at $t \geq t_{fin}$. As discussed in detail by Michaud and Månson, the rate at which the matrix advances into the fiber mat and the time needed for complete unloading of the fiber mat depend on the melt viscosity [37]. Rheological measurements reported elsewhere for the same iPP and iPP/MMT materials as those used in this work [35] show large viscosity increases in the low shear rate regime on MMT addition. However, iPP/MMT nanocomposites show significantly greater shear thinning than iPP at shear rates greater than 0.1 s^{-1}, so that at high shear rates the increase in viscosity is relatively small. It follows that longer times may be required for the complete unloading of the fiber mat as the MMT concentration increases, even if initial infiltration, which is associated with relatively high shear rates, is unaffected. The observed differences in fiber distribution were therefore attributed to incomplete unloading of the fibers in the matrix during the consolidation step for the MMT containing matrices. This does not account for the asymmetry in the fiber distributions in the presence of the MMT, but this is thought to be due to temperature differences between the top and bottom plates of the mold.

The values found for the tensile moduli of the GMT specimens are consistent with those calculated from Eq. 4 for a 3D random fiber orientation. This is in agreement with the results obtained by Wolfrath et al. [47], who also have found E for pure consolidated iPP GMT obtained by compression molding with a sufficiently long impregnation time to be close to the value calculated assuming a random 3D fiber orientation. The higher strain at break of the iPP GMT with respect to that of the iPP/MMT GMT composites is ascribed to the higher strain at break of the iPP matrix and to the observation that the glass fibers could be pulled out over greater lengths before breaking in the absence of MMT, so that the fibers bridged the fracture surfaces over longer distances and dissipated more energy than in the presence of MMT. The improved matrix–fiber adhesion observed in presence of MMT is expected to have a positive effect on the tensile strength. On the other hand, the MMT clusters may act as stress concentrators and hence offset any benefit from the improved matrix–fiber adhesion.

The decrease in E_b for the GMT specimens with MMT content, despite the increase in E_b shown for the compression molded matrix, was inferred to be due to the fiber volume fraction gradients present in the GMT composites containing MMT. This hypothesis was consistent with the results obtained from classical beam theory, and confirmed by the much higher E_b shown by set 4, which had a different fiber distribution, with most of the fibers concentrated in the outer layers of the specimens (see Fig. 2). The shape of the stress–strain curves and the results obtained for the strength and the elongation at break may be interpreted in the light of the fractographic analysis. Once a crack was generated at the surface of a three-point bend specimen, the extent of crack propagation at any given strain was significantly more limited in the iPP GMT, which had a relatively a homogeneous through-thickness fiber distribution, than in the iPP/MMT-based GMT. Energy dissipation due to fiber pull-out and/or crack bridging effectively hindered the propagation of the fracture throughout the thickness of the iPP GMT. On the other hand, the inhomogeneity of the fiber distribution in the iPP/MMT GMT resulted in matrix-rich regions in which crack onset and propagation was facilitated, and the presence of such regions at the specimen surfaces was apparently particularly detrimental to performance. The importance of the fiber distribution was clearly demonstrated by comparison of crack propagation for iPP5.4 GMT specimens with the standard and the modified stacking sequence. The presence of a fiber-rich surface layer in this latter case clearly retarded damage initiation, leading to a much higher flexural strength than with the standard stacking sequence, although the decrease in stress beyond the stress maximum was relatively abrupt, leading to qualitatively more brittle behavior. This may be explained at least in part by the reduced crack resistance in the matrix-rich specimen interior.

Conclusions

The principal effect of MMT addition to the matrix of iPP-based GMT composites was to modify the final fiber distribution, an observation that was accounted for in terms of the relatively high melt viscosity of iPP/MMT at low shear rates. Although they had relatively little influence on the tensile properties of the GMT, these changes in fiber distribution were reflected by significant changes in flexural properties. The low fiber contents at the surfaces of

standard lay-up GMT specimens containing MMT resulted not only in reduced flexural strength, owing to the relative brittleness of the matrix-rich areas at the outer surfaces, but also a reduction in the bending modulus, in spite of the increased matrix stiffness in the presence of MMT. This was corroborated by the behavior of specimens with lay-ups designed to increase their surface fiber contents, which resulted in markedly improved flexural modulus and strength. Such effects have direct consequences for industrial implementation of MMT-modified GMT because the latter stages of the fiber unloading process are expected to be insensitive to cycle time, iPP/MMT showing an exponential increase in melt shear viscosity with decreasing strain rate. Further work with the aim of assessing the effect of MMT addition on the impact toughness of iPP/MMT GMT composites is currently in progress and will be reported separately.

Acknowledgements We are grateful to the Centre Interdisciplinaire de Microscopie Electronique (CIME) of the EPFL and L. Mathieu, S. Lavanchy, and R. Ruggerone for their technical assistance.

References

1. Stokes VK (1995) J Eng Mater Technol 117:448
2. Karger-Kocsis J (2000) Polym Compos 21:514
3. Ericson M, Berglund L (1992) Compos Sci Technol 43:269
4. Ericson ML, Berglund LA (1993) Polym Compos 14:35
5. Ericson ML, Berglund LA (1993) Compos Sci Technol 49:121
6. Lee NJ, Jang JS (1999) Composites Part A 30:815
7. Lee NJ, Jang JS (2000) Compos Sci Technol 60:209
8. Stokes VK (1990) Polym Compos 11:32
9. Stokes VK (1990) Polym Compos 11:354
10. Zhao RF, Zhou XD, Dai G (2002) Polym Compos 23:1026
11. Lindhagen J, Berglund L (1998) J Appl Polym Sci 69:1319
12. Karger-Kocsis J, Harmia T, Czigány T (1995) Compos Sci Technol 54:287
13. Czigany T, Marosfalvi J, Karger-Kocsis J (2000) Compos Sci Technol 60:1203
14. Romhany G, Czigany T, Benevolenski OI, Karger-Kocsis J (2001) Adv Compos Lett 10:257
15. Benevolenski OI, Karger-Kocsis J (2001) Compos Sci Technol 61:2413
16. Benevolenski OI, Karger-Kocsis J, Czigany T, Romhany G (2003) Composites Part A 34:267
17. Karger-Kocsis J, Fejes-Kozma Z (1994) Mech Compos Mater 30:8
18. Karger-Kocsis J (1994) J Mater Sci Lett 13:1422
19. Balazs AC, Emrick T, Russell TP (2006) Science 314:1107
20. Tjong SC (2006) Mater Sci Eng R 53:73
21. Gilman JW, Kashiwagi TJ (2000) In: Pinnavaia TJ, Beall GW (eds) Polymer-clay nanocomposites. Wiley, Chichester, UK
22. Tsai JL, Wu MD (2007) J Compos Mater 41:2513
23. Aktas L, Altan MC (2010) Polym Compos 31:620
24. Tsai JL, Kuo JC, Hsu SM (2006) Mater Sci Forum 505–507:37
25. Tsai JL, Kuo JC, Hsu SM (2006) J Mater Sci 41:7406. doi: 10.1007/s10853-006-0800-6
26. Subramaniyan AK, Sun CT (2006) Composites Part A 37:2257
27. Norkhairunnisa M, Azhar AB, Shyang CW (2007) Polym Int 56:512
28. Haque A, Shamsuzzoha M, Hussain F, Dean D (2003) J Compos Mater 37:1821
29. Hussain F, Dean D, Haque A, Shamsuzzoha AM (2005) J Adv Mater 37:16
30. Ravindran N, Cho EH (2006) J Vinyl Addit Technol 12:25
31. Kornmann X, Rees M, Thomann Y, Necola A, Barbezat M, Thomann R (2005) Compos Sci Technol 65:2259
32. Akkapeddi MK (2000) Polym Compos 21:576
33. Zhao R, Huang J, Bin S, Dai G (2001) J Appl Polym Sci 82:2719
34. Houphouët-Boigny C (2007) Fiber reinforced polypropylene nanocomposites. PhD Thesis, Ecole Polytechnique Fédérale de Lausanne (EPFL), Lausanne
35. Houphouët-Boigny C, Plummer CJG, Dalle Vacche S, Michaud V, Wakeman MD, Månson JAE (2007) J Compos Mater 44:1075
36. Michaud V, Tornqvist R, Månson JAE (2001) J Compos Mater 35:1174
37. Michaud V, Månson JAE (2001) J Compos Mater 35:1150
38. Houphouët-Boigny C, Plummer CJG, Wakeman MD, Månson JAE (2007) Polym Eng Sci 47:1122
39. Gopakumar TG, Lee JA, Kontopoulou M, Parent JS (2002) Polymer 43:5483
40. Lingaiah S, Sadler R, Ibeh C, Shivakumar K (2008) Composites Part B 39:196
41. Park J, Eom K, Kwon O, Woo S (2001) Microsc Microanal 7:276
42. Cox HL (1952) Br J Appl Phys 3:72
43. Krenchel H (1964) Fibre reinforcement. Akademisk Forlag, Copenhagen
44. Thomason JL, Vlug MA (1996) Composites Part A 27:477
45. Matthews FL, Rawlings RD (1995) Composite materials: engineering and science. Chapman & Hall, London
46. Li J, Ton-That MT, Leelapornpisit W, Utracki LA (2007) Polym Eng Sci 47:1447
47. Wolfrath J, Michaud V, Månson JAE (2005) Polym Compos 26:361